Improved multipoint statistics method for reconstructing three-dimensional porous media from a two-dimensional image via porosity matching

Kai Ding, Qizhi Teng,* Zhengyong Wang, Xiaohai He, and Junxi Feng
College of Electronics and Information Engineering, Sichuan University, Chengdu 610065, China

(Received 3 January 2018; revised manuscript received 6 April 2018; published 22 June 2018)

Reconstructing a three-dimensional (3D) structure from a single two-dimensional training image (TI) is a challenging issue. Multiple-point statistics (MPS) is an effective method to solve this problem. However, in the traditional MPS method, errors occur while statistical features of reconstruction, such as porosity, connectivity, and structural properties, deviate from those of TI. Due to the MPS reconstruction mechanism that the voxel being reconstructed is dependent on the reconstructed voxel, it may cause error accumulation during simulations, which can easily lead to a significant difference between the real 3D structure and the reconstructed result. To reduce error accumulation and improve morphological similarity, an improved MPS method based on porosity matching is proposed. In the reconstruction, we search the matching pattern in the TI directly. Meanwhile, a multigrid approach is also applied to capture the large-scale structures of the TI. To demonstrate its superiority over the traditional MPS method, our method is tested on different sandstone samples from many aspects, including accuracy, stability, generalization, and flow characteristics. Experimental results show that the reconstruction results by the improved MPS method effectively match the CT sandstone samples in correlation functions, local porosity distribution, morphological parameters, and permeability.

DOI: 10.1103/PhysRevE.97.063304

I. INTRODUCTION

Three-dimensional (3D) microstructures have significant effects on the properties of porous media in reservoir modeling. In general, the 3D microstructure of porous media is required to simulate its flow and transport properties, which is mainly related to the morphological features of the pore—the shapes and sizes of the pores—and the connectivity—the way the pores are connected and the frequency of their interconnection [1,2]. There are two methods to reproduce 3D microstructures of porous media. The first method is based on instruments such as serial sectioning, x-ray computed microtomography (CT), focused ion beam (FIB), laser-scanning confocal microscopy, and scanning electron microscopy (SEM). In this approach, the 3D microstructures of porous media can be directly and accurately obtained. However, on the one hand, the high cost and unavailability of instruments limit the application of such methods. On the other hand, in contrast to 3D images, high-resolution two-dimensional (2D) sections of porous media can be obtained with relative ease. Hence the reconstruction of the microstructure of 3D heterogeneous materials from a 2D image is of great value in such cases. In the last few decades, several main reconstruction methods, i.e., process-based reconstruction [3], simulated annealing (SA) [4–7], texture synthesis [8–10], Gaussian random field [11], and multipoint statistics (MPS) [12–17] methods, have recorded considerable improvements.

Process-based reconstruction numerically emulates the growth of a porous medium on a computer. To obtain the porous medium structure by this method, adequate understanding of the physical or chemical mechanism that forms the microstructure is essential. However, this understanding is difficult to attain for some porous rocks, such as carbonates. Practical simulations have determined that the method is limited to simulating porous samples in a small size and with a short-range connectivity.

The Gaussian random field method proposed by Roberts *et al.* [11] aims at reconstructing statistically homogeneous and isotropic random media from the associated two-point correlation functions. However, although a variety of microstructures can be generated using this method, the morphological information in the reconstruction can be determined by the two-point correlation functions.

SA is an optimization technique based on the principle of metal annealing and inspired by the Monte Carlo methods in statistical mechanics. The SA algorithm enables the flexibility of combining multiple statistical descriptors to more effectively describe the spatial characteristics of random porous structures. A combination of different microstructural descriptors [18] has been successfully used to reconstruct several porous media, including sandstone and chalk. Furthermore, a global optimal solution in the process can be obtained such that the reconstruction result has the same statistical characteristics as the training image (TI). However, this approach is time consuming for the convergence of the objective function. Several methods have been presented to improve the performance of this method. Alexander *et al.* [19] proposed a hierarchical simulated annealing (HSA) method to reduce the computational cost such that more complex synthesis problems can be attempted on large images with multiple scales using this approach. Jiao *et al.* [20–22] introduced a lattice-point algorithm for efficiently reconstructing homogeneous and isotropic media and described an algorithm modification using

*Corresponding author: qzteng@scu.edu.cn

surface optimization to speed up the reconstruction process [23]. Gerke and Karsanina [24] introduced a way to weight correlation function input into the energy function, which improved both accuracy and convergence rate.

The texture synthesis method [8–10] has witnessed rapid development in recent years. It is an optimization method that considers the microstructure as a stationary Markov random field. The method mainly uses a global energy function to quantitatively measure the difference between the TI and the reconstructed 3D structure, and then minimize the energy function to obtain a synthesized high-quality texture. Nevertheless, the synthesized result mainly accounts for visual similarity with the TI, while seldom considering the consistency of statistical distributions.

The methods described above still cannot preserve morphological features and reproduce the flow characteristics of the complex porous media well. The MPS method, originally proposed by Guardiano and Srivastava [12], uses a template to capture connectivity and local morphological information. However, it is time consuming to scan the TI to obtain each new data event, thereby rendering this method impracticable. To address this problem, Strebelle *et al.* [25] proposed a single normal equation simulation (SNESIM) method in which all pattern types are stored by a search tree after the TI is scanned once. Therefore, it is feasible to apply SNESIM to 3D reservoirs. However, the SNESIM method suffers from large memory requirements of the large 3D reservoirs.

More recently, the direct sampling (DS) approach proposed by Mariethoz *et al.* [26,27] was shown to identify the pattern resembling the targeted data event most in the TI. The pattern can be directly pasted into the grid. However, it is difficult to adjust some parameters with this method. Tahmasebi *et al.* [28–32] proposed the cross-correlation–based simulation (CCSIM) method, in which the matching block is judged by a cross-correlation function together with a grid-splitting methodology. In this method, the computational speed and the accuracy of the simulated result can be greatly improved. A three-step sampling method presented by Gao *et al.* [33] generates the 3D structure by stacking a series of 2D images. In this method, it is crucial to control the continuity of the adjacent layers as well as the variability. The main advantage of the method is that connectivity can be preserved effectively.

However, in the traditional MPS method, one seldom considers the error accumulation, which may cause a great morphological difference between the TI and the reconstructed 3D structure, such as average volume of pore, average shape factor of pore, and average coordination number for sandstone materials. Moreover, due to the deficiency of the global statistic in the traditional MPS method, connectivity cannot always be captured dramatically.

To improve morphological similarity and strengthen stability in the reconstruction, an improved MPS method based on porosity matching is proposed to reduce error accumulation. For each reconstruction, we search the matching pattern in the TI directly, which is inspired by the texture synthesis [8–10] and the DS method [26,27]. The porosity matching scheme determines whether to correct the reconstructed voxel according to porosity deviation between the TI and the reconstructed 3D structure. A multigrid system is also used to capture the large-scale structures of the TI. Tests conducted on different sandstone samples demonstrate the accuracy, efficiency, stability, and generalization of the proposed method.

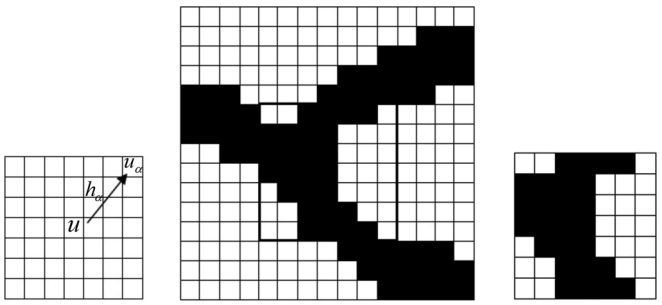

FIG. 1. Template and pattern: (a) template, (b) 15 × 15 TI, and (c) pattern.

The remainder of this paper is organized as follows. In Sec. II, we describe the traditional MPS algorithm, while the improved MPS method is presented in Sec. III. In Sec. IV, the performance of the proposed method is demonstrated. Conclusions are presented in Sec. V.

II. MULTIPOINT GEOLOGY STATISTICS METHOD

The SNESIM multipoint statistics method described in this section was proposed by Strebelle [19] in 2002. In this method, pattern information extracted from 2D TI is used to reconstruct the 3D structure. Since all patterns come from the TI, the TI must satisfy the stationary and Eigen assumption. Two main steps are used to generate a 3D model using a single TI: pattern set establishment and reconstruction.

To obtain the pattern, a searching template is used for scanning the TI. The searching template τ_n is composed of n locations h_α and a central location u:

$$\tau_n = \{h_\alpha, \alpha = 1,...,n\}. \tag{1}$$

Here h_α denotes the vectorized locations. Thus, the different positions can be defined as

$$u_\alpha = u + h_\alpha \quad \alpha = 1,...,n. \tag{2}$$

As shown in Fig. 1(a), the template size is 7 × 7 and the template includes 48 vectors. The TI shown in Fig. 1(b) is scanned using this template to obtain the pattern shown in Fig. 1(c). Therefore, by scanning the TI by the searching template, the pattern at each location u is obtained. The pattern is defined as

$$T(u) = \{i(u); i(u + h_\alpha), \alpha = 1,...,n\}, \tag{3}$$

where $i(u)$ denotes the pixel value of location u for a searching template. The pattern is determined by the pixel value of each location. Then a set is defined to store all patterns in the TI, which can be written as

$$V_{\text{set}} = \{T(u_i)\} \quad i = 1,...,m. \tag{4}$$

Here m denotes the number of voxels in the TI. Assuming that location u has K possible statuses $\{S_k, k = 1,2,...,K\}$, we

can obtain the simulated voxel by calculating the probability of occurrence of patterns u_α. The probability, also called the conditioning probability distribution function, is written as

$$P(i(u)=s_k|T_n)=\frac{P\{i(u)=s_k,i(u_\alpha)=s_\alpha\}}{P\{i(u_\alpha)=s_\alpha\}},\quad \alpha=1,\ldots,n, \tag{5}$$

where T_n denotes a specific pattern $i(u_\alpha)=s_\alpha$. For a specific status s_k $k=1,\ldots,K$, the probability of location u can be calculated by the condition $i(u_\alpha)=s_\alpha$. The equation can also be defined as

$$P(i(u)=s_k|T_n)=\frac{N\{i(u)=s_k,i(u_\alpha)=s_\alpha\}}{N\{i(u_\alpha)=s_\alpha\}},\quad \alpha=1,\ldots,n. \tag{6}$$

Here N is the number of a specific pattern. For the same conditioning data, the pixel value of location u_α is calculated as follows:

$$s_k=s_q|_{\max[N\{i(u)=s_k,i(u_\alpha)=s_\alpha\}]}\quad k,q=1,\ldots,K. \tag{7}$$

III. PROPOSED METHOD

A. Pattern matching

Similar to DS [26,27] and texture synthesis [8–10], we adopted a pattern-matching method that calculates the Euclidean distance between the searching pattern in the reconstructed 3D structure and the matching pattern in the TI. To preserve the local structure of the TI to the greatest extent, the errors for nearby pixels should be greater than those for distant pixels [8]. Thus, the Gaussian weighting function is used in the distance calculation. To this end, taking the x direction as an example, the function is defined as

$$e_{v,x}=\arg\min_{e_{v,x}}\sum_{u\in N_i(v)}G_{v,u}||s_{v,x}-e_{v,x}||^2. \tag{8}$$

Here e and s denote the TI and the reconstructed 3D structure, respectively, v and s_v indicate the voxel being reconstructed and the value of voxel v, respectively, and $s_{v,x}$ is the vectorized searching pattern of v in the slice orthogonal to the x axis. The pattern closest to $s_{v,i}$ is denoted by $e_{v,i}$ in the TI, as shown in Fig. 2; this is called the matching pattern.

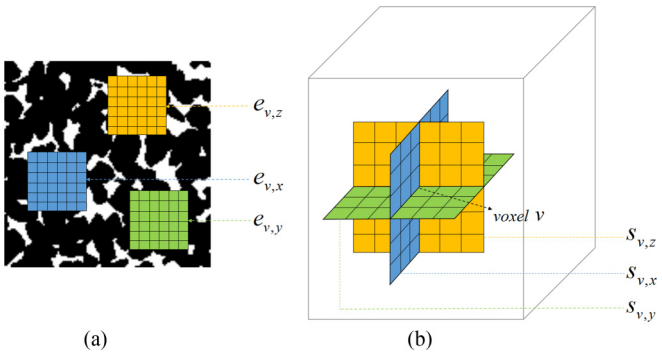

FIG. 2. Pattern matching: (a) TI and (b) simulated 3D structure.

In addition, $N_i(v)$ represents each location of the voxel in the searching pattern and matching pattern.

After directly searching the three matching patterns in the TI, we consider only the center pixels of the three matching patterns. If any two pixels belong to the same phase, we regard this phase as the reconstructed value.

The pattern-matching method based on Gaussian weighting Euclidean distance enables the corresponding pixels closer to the central voxel more similarity between the searching pattern and the matching pattern, such that the local similarity between the TI and the reconstructed 3D structure can be strengthened as much as possible. Moreover, this method can capture the connectivity of pore space, causing our reconstruction to be consistent with the CT sample in global connectivity.

B. Multiple-grid approach

In the MPS method, a multiple-grid simulation approach is used to capture the large-scale structures of the TI, in which a number of increasingly finer grids are simulated [25,34]. Moreover, Liu *et al.* [35] pointed out that a three-grid system is most suitable to obtain the best reconstruction performance after considering efficiency and accuracy. Thus, we herein adopt the three-grid system as shown in Fig. 3.

In a multigrid system, reconstruction is first performed on the third grid. Then, the reconstructed pixels are allocated to the corresponding grid nodes on the second grid, and these grid nodes are regarded as the conditioning data in the second grid reconstruction. The reconstruction in the third grid is the same as in the second grid.

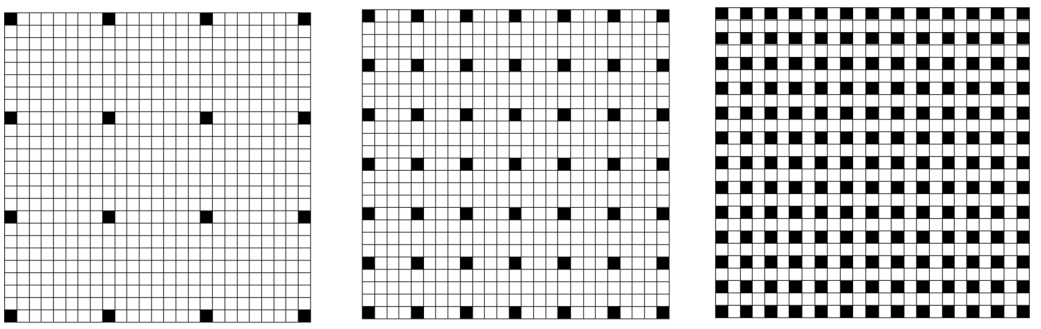

FIG. 3. Three-grid system: (a) the third grid, (b) the second grid, and (c) the first grid.

TABLE I. Procedure of the improved MPS method.

(1)	Initiate simulated structure S, set the multiple-grid system, $S_{\text{coarsest}}, S_{\text{finer}}, S_{\text{finest}}$;
(2)	For ($S == S_{\text{coarsest}}$; $S! = S_{\text{finest}}$; $S++$);
(3)	If ($S == S_{\text{coarsest}}$);
(4)	Select voxel v and calculate the searching patterns, $s_{v,i}$;
(5)	Search the matching patterns $e_{v,i}$ corresponding to $s_{v,i}$ in the TI;
(6)	Calculate the reconstructed voxel v;
(7)	Or else
(8)	Select voxel v and set a threshold, Num;
(9)	Count the conditioning data and reconstructed voxel $N_{v,i}$ for $s_{v,i}$;
(10)	Count the number l with $N_{v,i} > Num, i \in \{x, y, z\}$;
(11)	If ($l == 3$),
(12)	Search $e_{v,i}$ for each $s_{v,i}$ and then reconstruct v;
(13)	Or if ($l == 2$),
(14)	Search $e_{v,i}$ corresponding to $s_{v,i}$ with $N_{v,i} > Num$;
(15)	Calculate the shortest distance for $s_{v,i}$ and obtain the reconstructed voxel;
(16)	Or else
(17)	Repeat 8–17;
(18)	Porosity matching is immediately performed after the voxel is reconstructed each time.

It is notable that to fully leverage the conditioning data, we adopt different reconstruction methods to obtain accurate results. It can be classified into three different situations according to the amount of conditioning data and reconstructed voxel in each searching pattern. We set a threshold for the amount. If the conditioning data and reconstructed voxel in the three searching patterns respectively transcend the threshold, the grid node can be reconstructed by Eq. (8). If only two searching patterns meet the demand, we calculate the distances of the two matching patterns corresponding to the searching patterns. Then, the center pixel of the matching patterns of the shortest distance is used as the grid node. In the other case, the voxel being simulated is temporarily set aside. We loop until all grid nodes are simulated.

C. Porosity matching

The traditional MPS method mainly considers the local similarity without considering any global statistics between the reconstructed 3D structure and the TI in the reconstruction. The error accumulation in the process may cause significant differences in the global morphologies between the reconstructed 3D structure and the CT sample, such as porosity, connectivity, structural properties, and permeability.

To address this challenge, we present a porosity matching scheme that effectively reduces error accumulation and thereby strengthens global morphological similarity between our reconstruction and the CT sample. Porosity is a fundamental parameter to describe the reconstructed 3D structure. The proposed porosity matching scheme is a simple but effective method designed to make the porosity of the reconstructed 3D structure close to the TI. Specifically, we adjust the value of the reconstructed voxel according to Eq. (9) to ensure that the porosity of the constructed 3D structure matches the TI:

$$\overline{V} = \begin{cases} 1-V & V=1,\ \varphi_{\text{rec}} \geqslant (1+\sigma) \times \varphi_{\text{ori}},\ R < 0.5 \\ 1-V & V=0,\ \varphi_{\text{rec}} \leqslant (1-\sigma) \times \varphi_{\text{ori}},\ R \geqslant 0.5 \\ V & \text{else} \end{cases}, \tag{9}$$

where V and $\overline{V}$ respectively denote the value of the reconstructed voxel and the modified value of the reconstructed voxel; 0 and 1 represent the respective grain and pore phases; and P_{ori} P_{rec} respectively denote the porosity of the TI and the reconstructed 3D structure. In addition, σ is a threshold that represents a small difference in porosity between the reconstructed 3D structure and the TI. R represents the percentage of the pore phase in the cube neighborhood centered on the voxel being simulated.

The above formula reads as follows. We maintain the porosity of the 3D structure to update as the reconstruction progresses. If the current porosity P_{rec} of the 3D structure surpasses P_{ori} by an unacceptable value and the current value of the reconstructed voxel is pore phase, then we consider the cube neighborhood of the voxel being simulated. That is, if the percentage of the pore phase R is less than 0.5, we modify the reconstructed voxel from the pore phase (value 1) to the grain phase (value 0); otherwise the reconstructed voxel is unchanged. If the current P_{rec} is significantly lower than P_{ori} and the reconstructed voxel is the grain phase, and R is more than 0.5, we turn the grain phase to the pore phase according to Eq. (9) correspondingly. In the other case, porosity matching is not applied.

Porosity matching enables the global statistics of the 3D structure to match the TI, while pattern matching strengthens the local similarity. The integrated method automatically adapts to the current situation: if the porosity of the reconstructed 3D structure is far from the TI, we carry out porosity matching for the reconstructed voxel; otherwise the reconstruction switches to pattern matching only. The procedures of the improved MPS method are presented in Table I.

IV. RESULTS AND DISCUSSION

In this section, our method is tested on sandstone samples from several aspects, including correlation functions, local porosity distribution, morphological parameters, stability, generalization, and permeability.

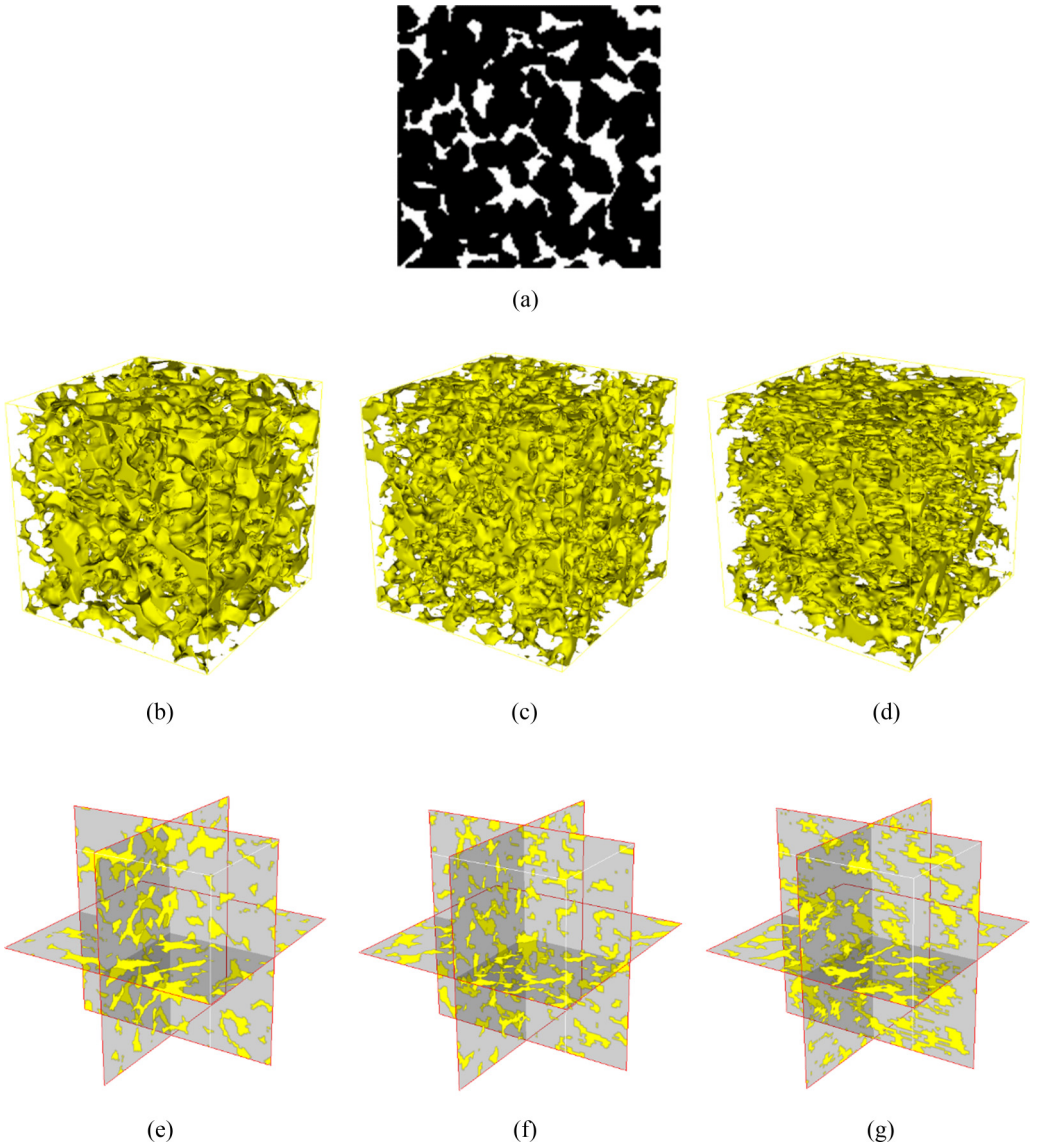

FIG. 4. Microstructures obtained from the CT sample of sandstone, the traditional MPS method, and the improved MPS method: (a) TI; (b) CT sample; (c) reconstructed result by the improved MPS method; (d) reconstructed result by the traditional MPS method; (e) 3D slice of the CT sample; (f) 3D slice of the reconstructed result by the improved MPS method; and (g) 3D slice of the reconstructed result by the traditional MPS method.

A. Results and correlation functions analysis

The 2D slice of a CT sandstone sample of 128 × 128 pixel size is handled as the TI, as shown in Fig. 4(a). It has a resolution of 10 μm. Black pixels correspond to grain and white pixels correspond to pore. The porosity of TI is close to that of the CT sample with 0.2001 and 0.1937, respectively. The perspective images of the CT sample, the reconstructed results by the improved MPS method, and the traditional MPS method proposed by Gao [33] are shown in Figs. 4(b)–4(d), respectively, and the 3D slices are shown in Figs. 4(e)–4(g). In the traditional MPS method and the improved method, the three-grid system is employed, and the template size used is 9 × 9 in our reconstruction. In the porosity matching scheme, the size of the cube neighborhood is 5 × 5 × 5 and the threshold σ is 0.05.

At the visual level, our reconstruction reproduces the structure and connectivity of the CT sample. However, it is not sufficient to determine the efficiency and accuracy of the proposed method. Thus, several approaches were used to present a more quantitative comparison between our reconstruction and the CT sample, and we also compared its performance with that of the traditional MPS method.

The autocorrelation function [1,36] is a fundamental descriptor and mainly indicates two-point distribution in random heterogeneous materials. The autocorrelation function of the pore phase in porous media is defined as

$$R(u) = \frac{\langle [I(r) - \phi][I(r+u) - \phi] \rangle}{\phi - \phi^2}. \tag{10}$$

Here r represents different locations within the porous media. In addition, $I(r)$ is a descriptor such that $I(r) = 1$ if r belongs to the pore space and $I(r) = 0$ in the other case. The porosity of the media is written as $\phi = \langle I(r) \rangle$.

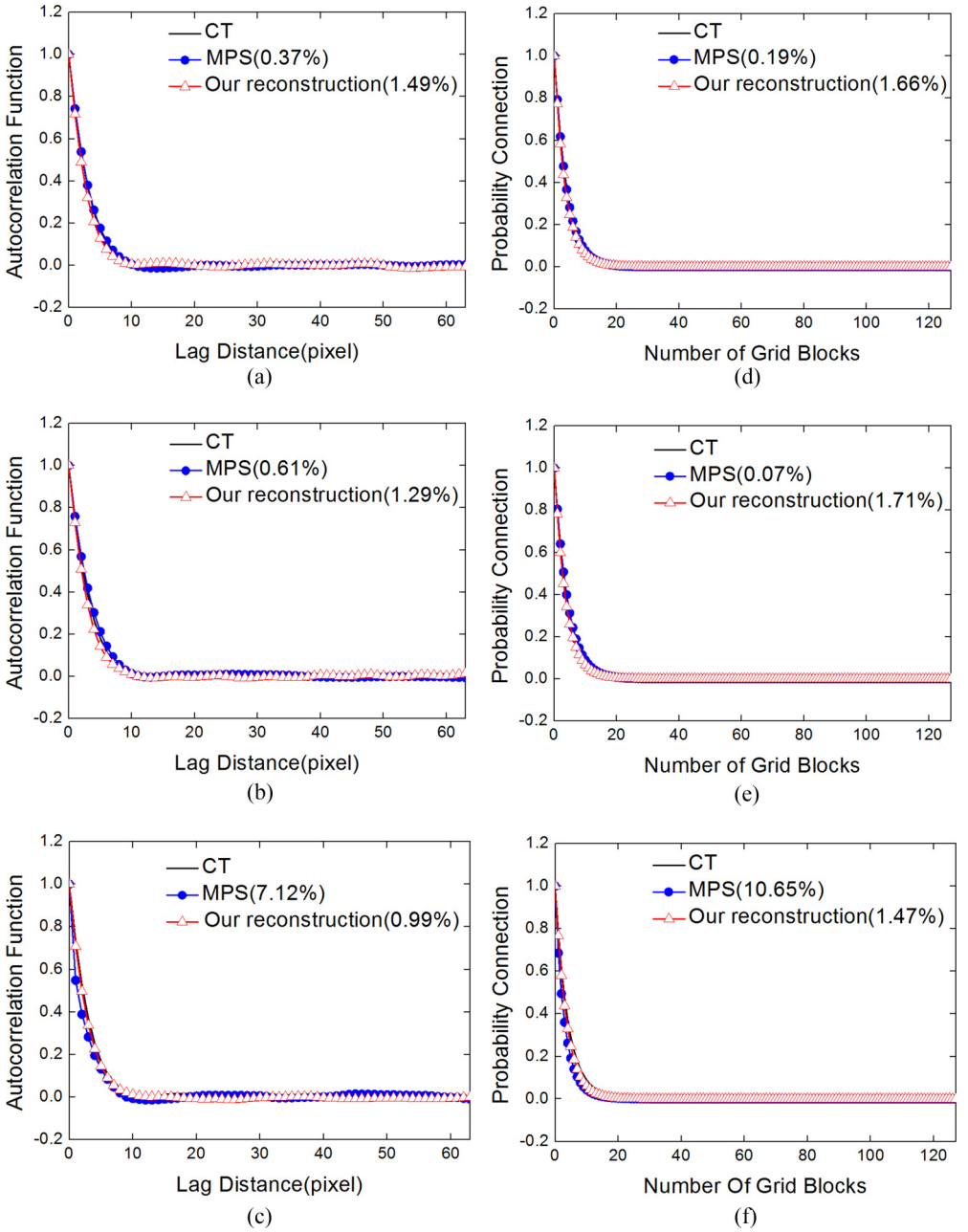

FIG. 5. Comparison of autocorrelation functions for the CT sample, reconstructed results of the traditional MPS method, and the improved MPS method in x, y, and z directions corresponding to (a)–(c), and the lineal path functions corresponding to (d)–(f). The numbers in parentheses indicate the L_2 norm errors.

The lineal path function, employed by Torquato and Lu [37,38], contains some topological connected information along a lineal path, thus partly reflecting connectedness information of a material system. The lineal path function measures the structural connectivity within a porous medium. The descriptor is concerned with the probability of selecting a vector $\vec{r}$ with each voxel located in one phase within the image. The lineal path function—the multipoint connectivity probability—is written as

$$L(\vec{u},\vec{u}+\vec{r}) = \begin{cases} 1 & \vec{r} \in V_0 \\ 0 & \text{else} \end{cases}. \tag{11}$$

The advantage of the lineal path function is that we can account for the curvilinearity of the system by considering a tolerance core around a given direction, which improves both characterization and, potentially, the reconstruction's accuracy [39,40].

We compared the autocorrelation functions and the lineal path functions of the CT sample, and the reconstructed results by the improved MPS method and the traditional MPS method in the three orthogonal directions. The curves of the comparisons are shown in Fig. 5. It is evident that the autocorrelation functions and the lineal path functions of the reconstructed results by the improved MPS method and the traditional MPS

method are in agreement with the CT sample in the three orthogonal directions.

B. Local porosity property

In this section, we compare the local porosity distribution [41,42] of the CT sample, the reconstructed results of the proposed method, and the traditional method. The local porosity is defined as

$$\phi(\vec{r},L) = \frac{N(P \cap K(\vec{r},L))}{N(K(\vec{r},L))}, \tag{12}$$

where unit $\mathrm{K}(\vec{r},L)$ is a cube centered at $\vec{r}$ with length L in a 3D image, P denotes one phase in the 3D image, and $\mathrm{N}(\mathrm{K}(\vec{r},L))$ represents the volume of unit $\mathrm{K}(\vec{r},L)$.

The local porosity distribution $\mu(\phi,L)$ is defined as

$$\mu(\phi,L) = \frac{1}{m}\sum_{\vec{r}} \delta(\phi - \phi(\vec{r},L)), \tag{13}$$

where m is the number of placements of the measurement cell $\mathrm{K}(\vec{r},L)$.

One unit with length L is set to scan the 3D sample to obtain the probability of different local porosities. The special length scale L is defined as

$$L = \min\{L : \mu(0,L) = \mu(1,L) = 0\}, \tag{14}$$

at which the δ distributions at $\phi = 0$ and 1 both vanish for the first time. In this place, $L = 21$.

The value of the local porosity and the probability of occurrence of the local porosity are represented by the x axis and y axis, respectively, as shown in Fig. 6.

Comparison of the local porosity distributions of the CT sample, the reconstructed results of the traditional MPS method, and the improved MPS method, are also presented in Fig. 6. In general, the local porosity distributions indicate some similarities in the changing trends for each sample. Peaks appear at the porosity between 0.19 and 0.21, which is similar to the porosity of the CT sample. In Fig. 6, the local porosity distribution of the reconstruction generated by the improved MPS method is much closer to that of the traditional CT sample.

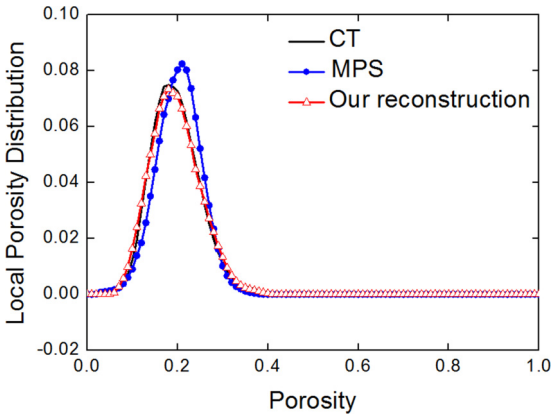

FIG. 6. Comparison of the local porosity distributions for the CT sample, reconstructed results of the traditional MPS method, and the improved MPS method.

C. Morphological parameters comparison

To verify the efficiency and accuracy of the proposed method in preserving the morphological features of the CT sample, we compared some important morphological parameters of the CT sample, the reconstructed results by the traditional MPS method, and the improved MPS, as presented in Table II.

It can be seen that the parameters of the morphological features generated by the improved MPS method are closer to the CT sample than those produced by the traditional MPS method. The error formula to calculate the deviation between the measured value and real value is

$$\delta = \frac{|L_1 - L_0|}{L_0} \times 100\%. \tag{15}$$

Here L_0 and L_1 represent real value and the measured value, respectively.

Table II presents a series of errors corresponding to different parameters. The average error of the improved MPS is 5.96%, which is significantly lower than the average error of 26.22% for the traditional MPS. This is because the porosity matching scheme promotes the generation of cluster structure and further strengthens the connectivity of the reconstructed result as the

TABLE II. Comparison of morphological parameters of the CT sample, reconstructed results of the traditional MPS method, and improved MPS method.

	Micro-CT	Traditional MPS	Improved MPS	Error of traditional MPS	Error of improved MPS
Porosity	0.1937	0.1947	0.1993	0.52%	2.89%
Average diameter of pore equivalent sphere (μm)	41.3	30.1	45.6	27.12%	10.41%
Average volume of pore (μm^3)	2.46×10^5	1.15×10^5	2.29×10^5	53.44%	6.90%
Average diameter of the smallest ball of pore (μm)	78.6	51.5	88.7	34.48%	12.85%
Average surface area of pore (μm^2)	2.37×10^4	1.38×10^4	2.49×10^4	42.03%	5.06%
Average shape factor of pore	0.66	0.73	0.60	10.61%	9.09%
Average pore-throat ratio	1.01	0.69	1.08	31.68%	6.93%
Average longest diameter of throat section (μm)	56.4	49.1	56.7	12.94%	0.53%
Average coordination number	2.24	1.51	2.30	32.59%	2.68%
Average cross-sectional area of throat (μm^2)	1925	1602	1882	16.78%	2.23%

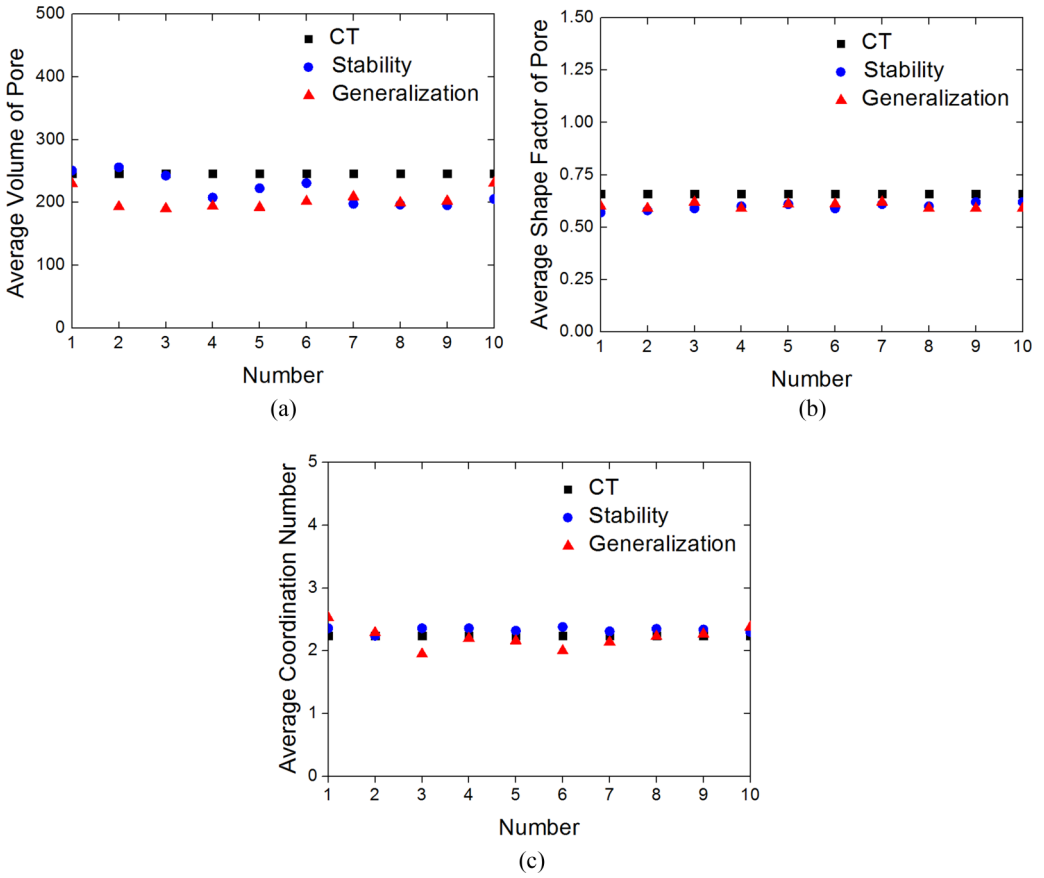

FIG. 7. Comparison of the average volume of pore in (a) the average shape factor in (b) and the average coordination number in (c) among ten sets of microstructures from the same TI, ten sets of microstructures from ten different slices, and the CT sample.

reconstruction progresses. Due to error accumulation in the process, the traditional MPS method yields huge morphological differences between our reconstruction and the CT sample. The sets of errors indicate that our method is efficient and accurate in maintaining the connectivity and morphological features of the CT sample, thereby demonstrating immense superiority over the traditional MPS method.

D. Stability and generalization

Thanks to the porosity matching scheme, the stability of our algorithm in reproducing the morphology can be ensured. To demonstrate this, we reconstructed ten microstructures of 3D sandstone from the same TI. In addition, to verify the generalization of the proposed method, ten different slices are randomly chosen as TI and are respectively used to reconstruct the corresponding 3D microstructures. A comparison of three important morphological parameters (average volume of pore, average shape factor of pore, and average coordination number) is shown in Fig. 7.

It can be clearly seen that three morphological parameters of the proposed method slightly fluctuate around those of the CT sample in Fig. 7. Therefore, slight changes of those morphological parameters indicate the accuracy, stability, and generalization of the proposed method. It is known that the average pore volume and average pore shape factor are relevant to the sizes and shapes of the pores, and the average coordination number is related to connectivity. Moreover, flow and transport properties of porous media are mainly dependent on the distribution of pore sizes, pore shapes, and the 3D spatial connectivity of a porous medium. According to those parameters, we can infer roughly that our reconstruction has similar flow and transport properties to the CT sample. To prove that, flow characteristics simulation is carried out in the next section.

E. Flow characteristics

To verify the effectiveness of our algorithm in reproducing the flow and transport characteristics of porous media, the permeabilities for single-phase flow and two-phase flow of the reconstructed results are tested in this section.

We first utilized the free software Finite-Difference Method Stokes Solver (FDMSS), which was proposed by Gerke [43], to obtain the absolute permeability. FDMSS provided a computationally efficient and accurate basis for single-phase pore-scale flow simulations and it solved the Stokes equation using a finite-difference method (FDM) directly on voxelized 3D pore geometries. The absolute permeabilities of the CT sample, the traditional MPS method, and our reconstruction were 1156 mD, 841 mD, and 1095 mD, respectively, according to this method. It can be seen that the absolute permeability of our reconstruction is in accordance with that of CT sample.

To further obtain the relative permeability, we adopted the method introduced by Dong and Blunt [44], who used the maximal ball algorithm to extract the sizes of the pores

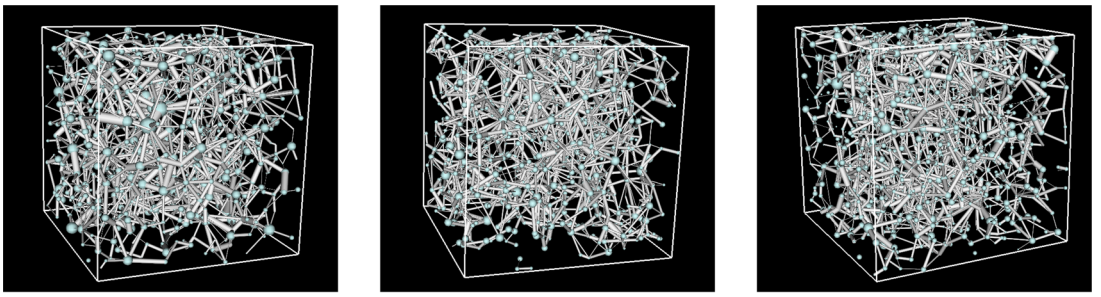

(a) (b) (c)

FIG. 8. Pore-throat network model: (a) the pore-throat network model of the CT sample; (b) the pore-throat network model of a reconstructed result by the traditional MPS method; and (c) the pore-throat network model of the improved MPS method.

and throats from images of a porous medium. This algorithm was developed to extract topologically disordered networks of pores and throats with parametrized geometry and interconnectivity. Herein we mainly used Valvatne's code [45] for simulations, and the pore-throat network model as shown in Fig. 8.

The two-phase flow simulation was divided into two procedures: the primary drainage displacement of a nonwetting phase (oil) by the wetting phase (water) and the reverse imbibition process. The oil and water densities were assumed to be 900 and 1000 kg/m^3, respectively, and the water-oil surface tension was assumed to be 3×10^{-2} N/m; the oil and water viscosities were assumed to be 1.05×10^{-3} and 1.0×10^{-3} kg/ms, respectively. In the first step, the pore-throat network is supposed to be wetted by the wetting phase, with a receding contact angle of 0° and an advancing contact angle of 0°. In the following step, the receding contact angle was set to 50° and the advancing contact angle was set to 60°.

The trends of oil and water relative permeability in drainage and imbibition processes are shown in Figs. 9(a) and 9(b), respectively. It can be seen that relative permeabilities of our reconstruction and the traditional MPS method match those of the CT sample well. In summary, the proposed method can reproduce the flow and transport characteristics of CT sample well, thus demonstrating that our reconstruction has statistical equivalent properties to that of CT sample and can be used for simulating the flow properties in reservoir modeling.

V. CONCLUSION

In this paper, we presented an improved MPS method using a 2D slice to reconstruct 3D porous media. A Gaussian weighting pattern-matching method was applied to the proposed method to strengthen the spatial structure similarity of the reconstructed result. A global porosity matching scheme was additionally proposed to reduce error accumulation and thereby ensure the accuracy and stability of our method.

Several approaches were used to verify the effectiveness of the improved MPS method. We compared its performance with that of the traditional MPS method. Visual comparison showed that it was feasible for our method to capture the connectivity of the CT sample. With respect to correlation functions, such as the autocorrelation function and lineal path function, the reconstructed result was consistent with the CT sample. Measurement of the local porosity distribution showed that our method reproduced the characteristic structure of the pore space. Comparisons of morphological parameters demonstrated that our method precisely captured the morphological features of the CT sample, thereby demonstrating its immense superiority over the traditional MPS method. Furthermore, our algorithm maintained a solid stability and good generalization. Analysis of permeability showed that our algorithm can reproduce flow and transport properties successfully and thereby can be applied to simulating the flow characteristics in reservoir modeling.

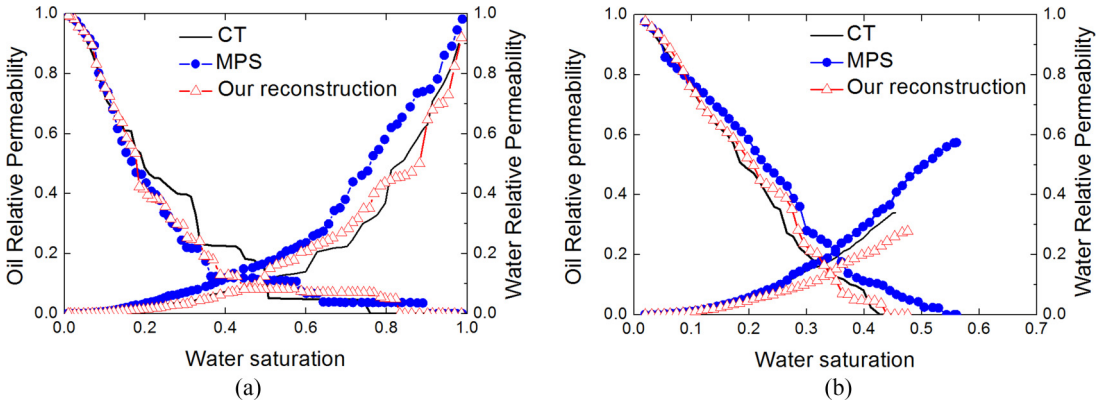

FIG. 9. Comparison of relative permeability among the CT sample, the traditional MPS method, and the improved MPS method: (a) drainage and (b) imbibition.

Several experiments verified the performance of our method. Considering its accuracy and stability, we aspire for its application to be widespread. However, because of direct searching of the matching pattern in the TI for each simulation, our method is more time consuming than the traditional MPS method. Therefore, further research should be conducted to reduce the time consumption of this method. In addition, other global statistics can be investigated to reduce error accumulation.

ACKNOWLEDGMENT

This work was supported by the National Natural Science Foundation of China (Grant No. 61372174).

[1] P. M. Adler, *Porous Media: Geometry and Transports* (Butterworth/Heinemann, London, 1992).
[2] M. Sahimi, *Flow and Transport in Porous Media and Fractured Rock*, 2nd ed. (Wiley-VCH, Weinheim, Germany, 2011).
[3] J. P. Latham, A. Munjiza, and Y. Lu, Powder Technol. **125**, 10 (2002).
[4] C. L. Y. Yeong and S. Torquato, Phys. Rev. E **57**, 495 (1998).
[5] C. L. Y. Yeong and S. Torquato, Phys. Rev. E **58**, 224 (1998).
[6] D. D. Chen, Q. Z. Teng, X. H. He, Z. Xu, and Z. J. Li, Phys. Rev. E **89**, 013305 (2014).
[7] M. Gao, Q. Teng, X. He, C. Zuo, and Z. J. Li, Phys. Rev. E **93**, 012140 (2016).
[8] J. Kopf, C. W. Fu, D. Cohen-Or, O. Deussen, D. Lischinski, and T. T. Wong, Proc. SIGGRAPH **26**, 2 (2007).
[9] V. Kwatra, I. Essa, A. Bobick, and N. Kwatra, Proc. SIGGRAPH **24**, 795 (2005).
[10] J. Chen and B. Wang, Visual Computer **26**, 253 (2010).
[11] A. P. Roberts, Phys. Rev. E **56**, 3203 (1997).
[12] F. B. Guardiano and R. M. Srivastava, in *Geostatistics–Troia'92*, edited by A. Soares (Kluwer Academic, Amsterdam, 1993), Vol. 1, pp.133–144.
[13] A. G. Journel, Math. Geol. **34**, 573 (2002).
[14] A. Hajizadeh, A. Safekordi, and F. A. Farhadpour, Adv. Water Resour. **34**, 1256 (2011).
[15] S. Strebelle and C. Cavelius, Math. Geosci. **46**, 171 (2014).
[16] H. Okabe and M. J. Blunt, Water Resour. Res. **43**, 179 (2007).
[17] A. Comunian, P. Renard, and J. Straubhaar, Comput. Geosci. **40**, 49 (2012).
[18] C. Manwart, S. Torquato, and R. Hilfer, Phys. Rev. E **62**, 893 (2000).
[19] S. K. Alexander, P. Fieguth, M. A. Ioannidis, and E. R. Vrscay, Math. Geosci. **41**, 357 (2009).
[20] Y. Jiao, F. H. Stillinger, and S. Torquato, Phys. Rev. E **76**, 031110 (2007).
[21] Y. Jiao, F. H. Stillinger, and S. Torquato, Phys. Rev. E **77**, 031135 (2008).
[22] Y. Jiao and N. Chawla, J. Appl. Phys. **115**, 093511 (2014).
[23] L. M. Pant, S. K. Mitra, and M. Secanell, Phys. Rev. E **90**, 023306 (2014).
[24] K. M. Gerke and M. V. Karsanina, Europhys. Lett. **111**, 56002 (2015).
[25] S. Strebelle, Math. Geol. **34**, 1 (2002).
[26] G. Mariethoz, P. Renard, and J. Straubhaar, Water Resour. Res. **46**, W11536 (2010).
[27] E. Meerschman, G. Pirot, and G. Mariethoz, Comput. Geosci. **52**, 307 (2013).
[28] P. Tahmasebi and M. Sahimi, Phys. Rev. Lett. **110**, 078002 (2013).
[29] P. Tahmasebi and M. Sahimi, Phys. Rev. E **85**, 066709 (2012).
[30] P. Tahmasebi and M. Sahimi, Comput. Geosci. **16**, 779 (2012).
[31] P. Tahmasebi and M. Sahimi, Water Resour. Res. **52**, 2074 (2016).
[32] P. Tahmasebi and M. Sahimi, Water Resour. Res. **52**, 2099 (2016).
[33] M. L. Gao, X. H. He, Q. Z. Teng, C. Zuo, and D. D. Chen, Phys. Rev. E **91**, 013308 (2015).
[34] T. T. Tran, Comput. Geosci. **20**, 1161 (1994).
[35] Y. H. Liu, Comput. Geosci. **32**, 1544 (2006).
[36] E. S. Kikkinides and V. N. Burganos, Phys. Rev. E **59**, 7185 (1999).
[37] S. Torquato and H. Haslach, Appl. Mech. Rev. **55**, B62 (2002).
[38] B. Lu and S. Torquato, Phys. Rev. A **45**, 922 (1992).
[39] K. M. Gerke, M. V. Karsanina, R. V. Vasilyev, and D. Mallants, Europhys. Lett. **106**, 66002 (2014).
[40] M. V. Karsanina, K. M. Gerke, E. B. Skvortsova, and D. Mallants, Plos One **10**, e0126515 (2015).
[41] R. Hilfer, Phys. Rev. B **45**, 7115 (1992).
[42] B. Biswal, C. Manwart, and R. Hilfer, Physica A **255**, 221 (1998).
[43] K. M. Gerke, R. V. Vasilyev, S. Khirevich, D. Collins, M. V. Karsanina, T. O. Sizonenko, D. V. Korost, S. Lamontagne, and D. Mallents, Comput. Geosci. **114**, 41 (2018).
[44] H. Dong and M. J. Blunt, Phys. Rev. E **80**, 036307 (2009).
[45] P. H. Valvatne and M. J. Blunt, Water Resour. Res. **40**, 187 (2004).